Chapter 9

# Laser Processing of Silicon for Synthesis of Better Biomaterials

Candace Colpitts and Amirkianoosh Kiani

Additional information is available at the end of the chapter

http://dx.doi.org/10.5772/intechopen.69856

**Abstract**

The increasing demand for new biomaterials and fabrication methods provides an opportunity for silicon to solve current challenges in the field. Laser processing is becoming more common as the public begins to understand its simplicity and value. When an abundant material is paired with a reliable and economic fabrication method, biomedical devices can be created and improved. In this chapter, different laser parameters of the Nd:YAG laser are investigated and the topographic and physical trends are analyzed. The biocompatibility is assessed for scanning speed, line spacing, overlap number, pulse frequency, and laser power with the use of simulated body fluid (SBF) and fibroblast culturing (NIH 3T3). Not only can nanosecond pulses increase the biocompatibility of silicon by generating silicon oxide nanofibers, but the substrate becomes bioactive with the manipulation of cell interactions.

**Keywords:** silicon, nanofibers, Nd:YAG laser, fibroblasts

## 1. Introduction

Science fiction has motivated intelligent minds to enhance the quality of living for the last century. A well-known example in fantasy is bionic limbs controlled by the mind. Individuals who have lost or permanently damaged limbs can benefit from procuring an aesthetically pleasing and fully functioning bionic replacement to restore or improve their quality of life. The field of biomaterials engineering has been making monumental advances by producing devices such as biosensors, bioMEMS, and artificial hearts [1–3]. There is a continuous growth in population today, demanding the attention from biomedical fields to improve lifestyles and create better body functionality. Although current devices' interfaces with the human body have come a long way, there is still a long way to go in the fabrication methods of the required scaffolds.

This chapter outlines one single pathway of research done to broaden the opportunities in the biomaterials industry. The bioactivity of laser-treated silicon is investigated through the use of *in vitro* testing. This research investigates of the trends of different laser parameters, including power, frequency, scanning speed, line spacing, and overlap number.

### 1.1. Challenges in the biomaterials industry

The current challenges in the biomedical field include finding biocompatible and bioactive organic or inorganic materials and simplifying manufacturing processes. Devices that are implanted inside the body require materials that are biocompatible; the behavior of this material when interacting with the human body must not have any toxic effects and must perform a specific task. For a material to be bioactive, it requires to be biocompatible and have a biological effect and provoke a positive and controlled biological response. Current biocompatible materials that are commonly used are gold, titanium, polymers, bioceramics, and composites [4–8].

Silicon was chosen as the material for this research due to its abundance and semiconductor abilities. Microfabricated silicon is widely used today in the microelectronics and photovoltaics industry [9, 10]. Silicon in its pure form is not biocompatible [11, 12]. However, silicon can be packaged in a biocompatible material such as titanium [13, 14]. It has been found that porous silicon is biocompatible [11]. The current method used for creating a porous layer is etching with hydrochloric acid. Acid etching is a long process that requires the use of dangerous chemicals and is consequently environmentally friendly. The challenge that silicon faces in the biomaterials industry is to find a superior surface alteration method.

### 1.2. Laser processing

Technology that easily controls and creates an accurate pattern on a microscale is required in the microelectronics industry. A good solution to this criterion is a laser, which has been commonly used for surface texturing of steel [15, 16]. It was found that this method of surface treatment allowed the generation of micropores with different characteristics. Unlike acid etching, a laser is great for the modification of silicon since it is very clean, high resolution, and controllability of intensity and depth of penetration. The Nd:YAG pulsed laser is a particularly good solution since it is cost-effective, stable, and has the required high power range. Another advantage to this method is that there are no chemicals involved, which eliminates the complex processes of preparation and environmental concerns. Above all, using a laser is a single-step process. The economic and simplistic benefits that are associated with this approach are valuable to the biomedical industry.

High-end picosecond and femtosecond pulsed laser systems have also been used for generation of porous silicon particles [17, 18]. In this research, it is found that a Nd:YAG nanosecond pulse laser can achieve the desired biocompatible silicon. The nanosecond laser is much more economical and commercially available than the faster pulse lasers. The nanosecond laser is also currently used in the medical industry for procedures such as eye and dental surgeries [19, 20].

## 2. Laser processing and surface characterization

Microfabrication with lasers is becoming increasingly popular in many industries including biomaterials [21]. Laser irradiation introduces surface irregularities and chemical changes to the silicon surface. The laser irradiates a simple line pattern onto pure silicon with <100> orientation. There are a number of methods used to analyze the condition of the laser-processed substrat. Images of the samples are taken with field emission scanning electron microscopy (FESEM) and 3D optical microscopy.

### 2.1. Laser system

The laser used in this research is a SOL-20 1064 nm Nd:YAG nanosecond laser by Bright Solutions Inc. The JD2204 Sino Galvo two-axis Galvo scanner has an input of 10 mm and a beam displacement of 13.4 mm. The theoretically determined spot size diameter is 19 μm. The laser pulses can range from lengths of 6 to 35 ns, frequencies of 10 to 100 kHz, powers up to 20 W, and scanning speeds up to 3000 mm/s. For this research, scanning speeds of 100–1000 mm/s, powers of 7, 10, and 15 W, and frequencies of 25, 70, and 100 kHz are used. Line spacing varies from 0.025, 0.05, and 0.10 mm. Overlap number, or number of times the laser repeats the same pattern, varies from 1, 2, and 3. The manipulation of these parameters is easily executed through the laser-operating software.

### 2.2. Biocompatibility evaluation

The biocompatibility of a material is influenced by surface roughness, reflectivity, and chemical content of the substrate. The chemical content is assessed using micro-Raman and energy-dispersive X-ray (EDX) analysis. The surface roughness is determined with the use of 3D optical microscopy, and the reflectivity is determined with light spectroscopy. The biocompatibility is also determined with the use of simulated body fluid, which is a form of *in vitro* assessment—testing done outside of the body. Simulated body fluid is a solution that mimics the ion concentration of human blood plasma. When a biocompatible material is submerged in the liquid, hydroxyapatite forms on the surface [22, 23]. The submerged samples in the SBF are kept in an incubator at 36.5°C for up to 6 weeks.

Cell interactions with the laser-processed silicon substrate are also evaluated with cultured mouse embryonic fibroblasts (NIH 3T3). Cells are seeded at 2400 cells/cm$^2$ in triplicate and incubated for 72 h at 37°C. The samples are incubated under 5% $CO_2$ in Dulbecco's modified Eagle medium (DMEM) supplemented with 10% heat-inactivated calf serum. Phosphate-buffered saline (PBS) was then used to rinse the nonadherent cells from the samples overnight at 4°C. Staining was then done to the samples with phalloidin (1:2000 dilution) and draq5 (1:10,000 dilution) overnight for fluorescence imaging.

### 2.3. Temperature evaluation

Different frequencies, powers, and pulse widths change the behavior of the laser pulses. Determining the temperature will help investigate the pulse energy and how it affects the

surface topographic properties and chemical structure. The surface temperature is modeled using the two-dimensional heat equation in cylindrical coordinates. The heat equation in cylindrical coordinates is found in Eq. (1).

$$\frac{1}{r}\frac{\partial}{\partial r}\left(\kappa r\frac{\partial T}{\partial r}\right)+\frac{1}{r^2}\frac{\partial}{\partial \phi}\left(\kappa\frac{\partial T}{\partial \phi}\right)+\frac{\partial}{\partial z}\left(\kappa\frac{\partial T}{\partial z}\right)+\dot{q}=\rho c_p\frac{\partial T}{\partial t} \tag{1}$$

where $\kappa$ is the heat conduction coefficient, $\rho$ is the material density (kg/m$^3$), $c_p$ is the specific heat (J/kgK), and $\dot{q}$ is the rate at which energy is generated per unit volume of the medium (W/m$^3$) [24]. Since it is assumed that $\kappa$, $\rho$, and $c_p$ are constant, and there is no energy generation within the silicon ($\dot{q}=0$), Eq. (1) can be simplified into Eq. (2).

$$\frac{1}{r}\frac{\partial}{\partial r}\left(r\frac{\partial T}{\partial r}\right)+\frac{\partial}{\partial z}\left(\frac{\partial T}{\partial z}\right)=\frac{1}{a}\frac{\partial T}{\partial t} \tag{2}$$

where $a = \kappa/\rho c_p$, which is the thermal diffusivity (m$^2$/s). The boundary conditions for this equation include the initial temperature being room temperature, the pulse intensity is at its maximum during the pulse at $z = 0$, the intensity is zero between pulses, and the temperature change is zero at $r = \infty$, and $z = \infty$. With these conditions, the single-pulse temperature change of a high absorption material, $\Delta T$, for a square pulse, can be obtained (Eq. (3)) [25].

$$\Delta T(r,z,\tau)=\frac{I_{max}\gamma\sqrt{\kappa}}{\sqrt{\pi}K}\int_0^{\tau}\frac{1}{\sqrt{t}\left[1+\frac{8\kappa t}{W^2}\right]}e^{-\left[\frac{z^2}{4\kappa t}+\frac{r^2}{4\kappa t+\frac{1}{2}W^2}\right]}dt \tag{3}$$

$$\text{where } I_{max}=\frac{P_{peak}}{A}=\frac{4P_{measured}}{\pi d^2 f\tau} \tag{4}$$

where $I_{max}$ (Eq. (4)) is the peak intensity which is the peak power divided by the spot area, $P_{measured}$ is the experimental measured power, $f$ is the pulse frequency, $\tau$ is the pulse duration, $\gamma$ is equal to the Fresnel energy reflectivity (R) subtracted from 1 (1–R) with a R value of 0.325 and a $\gamma$ value of 0.675, $\kappa$ is Silicon's diffusivity with a value of $9.07\times10^{-3}$ m$^2$/s, $K$ is Silicon's conductivity with a value of 155 W/mK, $\tau$ is the laser pulse duration, $W$ is the beam's filed radius (1/e) with a value of $1.94\times10^{-5}$ m, $z$ is the ablation pit depth, and $r$ is the ablation pit radius. Using this equation with the assumption that the pulse is square-shaped, the temperature can be determined at the center of ablation (r = 0) and at the surface (z = 0). From Eq. (3), an analytical expression can be made to determine the depth of the ablated groove at the center of the ablation with respect to radius by using the mean value theorem.

$$h(r)=\sqrt{-4\kappa\tau\ln\left\{\frac{\beta K\Delta T_B}{\gamma I_{max}}\sqrt{\frac{\pi}{\kappa\beta\tau}}\left(1+\frac{8\beta\kappa\tau}{W^2}\right)\right\}-\frac{r^2}{1+\frac{W^2}{8\beta\kappa\tau}}}\leq h(0) \tag{5}$$

where $\beta$ is an experimentally determined correction factor of 0.5 and $\Delta T_B$ is silicon's boiling temperature of 2972 K. A more accurate representation of the experimental results found in

Eqs. (6) and (7) will determine the ablation depth after a train of pulses. Each consecutive pulse adds to the penetration of the preceding pulse, $S$, resulting in a deeper groove.

$$h_{scan}(r) = h(r) + h(S - r) \tag{6}$$

$$S = \frac{v\_scan}{f} \tag{7}$$

where $S$ is the spatial separation between each consecutive pulse, $v\_scan$ is the scanning speed in m/s, and $f$ is the pulse frequency.

## 3. Effect of scanning parameters

The three scanning parameters discussed in this section are overlap number, line spacing, and scanning speed. Each of these is easily set through the laser-operating software. These parameters have a direct effect of the surface topography and oxidation levels of the silicon substrates.

### 3.1. Topography analysis

The field emission scanning electron microscope images are an effective way of investigating the physical results from the laser ablation on the silicon samples. **Figure 1** shows the effect of different overlap numbers. At 1 overlap (OL), the line pattern is distinct and relatively clean. When the OL number is increased to 2, the line pattern is less definite and contains more irregularities. Finally, increasing the overlap number once again to 3, the line pattern is almost unrecognizable with a substantial amount of imperfections.

The effect of different line spacing was then investigated with FESEM. The overlap number was kept constant at 1. At the largest line spacing of 0.10 mm, the line pattern is discrete. At the smallest line spacing of 0.025 mm, the amount of imperfections is high with no distinctive line separation. The effect of line spacing can be seen in **Figure 2**.

Knowing that a higher overlap number and a smaller line spacing made for the highest level of laser-ablated substrate, a sample with 0.025 mm line spacing and three overlaps was created to observe the surface characteristics. The high magnification FESEM image in **Figure 3** of this sample shows a nanofibrous substrate. These nanofibers are the result of a high-energy reactive plume that forms on the surface during laser ablation [26]. The plume generates a heat-affected zone that causes the silicon ions to react with the oxygen ions, creating these nanoscale $SiO_2$ fibers [27–29].

The effect of scanning speed was then investigated with 3D optical microscopy. The data of the results from scanning speeds of 100, 200, 500, 800, and 1000 mm/s are mapped and compared in **Figure 4**. It is expected that the lower scanning speeds have larger depths due to a higher number of pulses ablating the surface area. However, with a closer look at **Figure 4**, the lower scanning speeds have shallow depths and a relatively high wall of built-up material along the

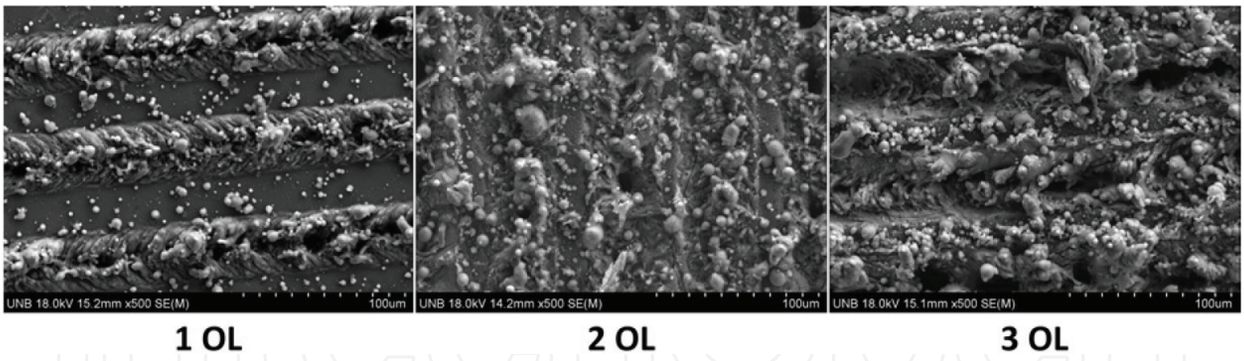


**Figure 1.** FESEM images of pattern overlaps of 1, 2, and 3 with a line spacing of 0.10 mm, a laser power of 10.5 W, a frequency of 100 kHz, and a scanning speed of 400 mm/s.

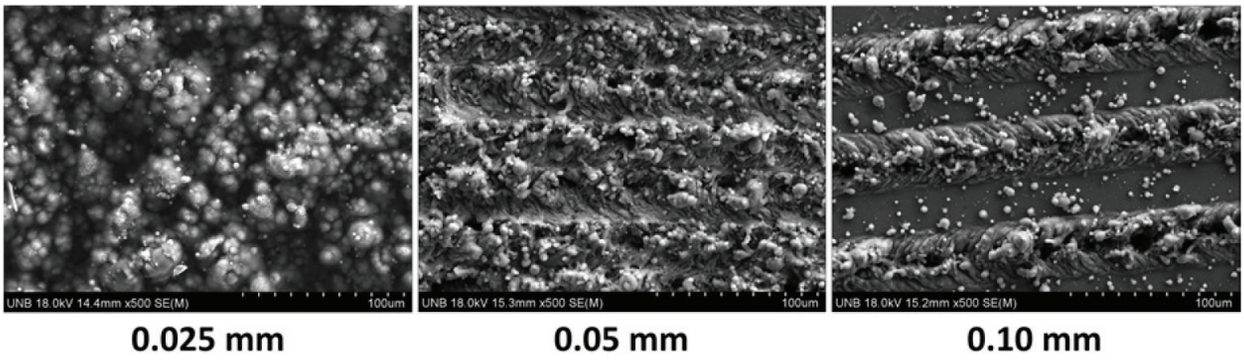


**Figure 2.** FESEM images of line spacing of 0.025, 0.05, and 0.10 mm with an overlap number of 1, a laser power of 13.3 W, a frequency of 100 kHz, and a scanning speed of 400 mm/s.

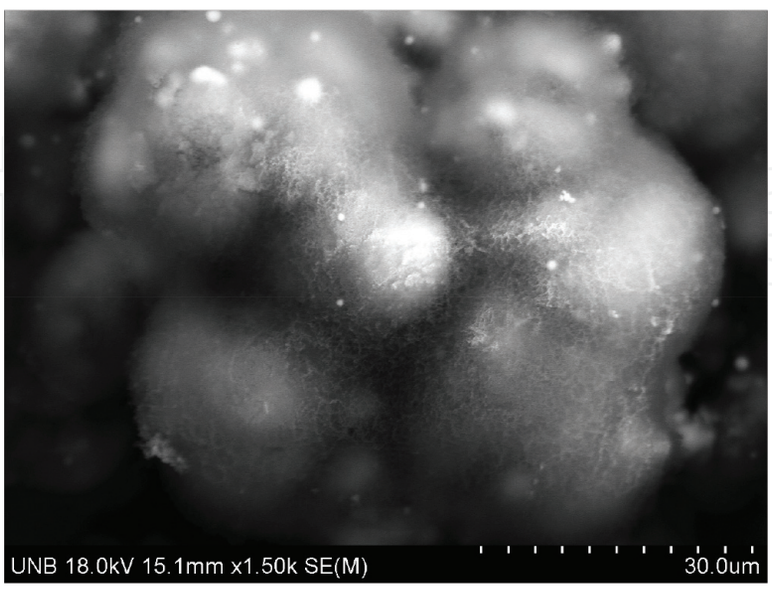


**Figure 3.** Presence of nanofibers detected on FESEM image of sample with three overlaps and 0.025 mm line spacing with power of 13.3 W, frequency of 100 kHz, and a scanning speed of 400 mm/s.

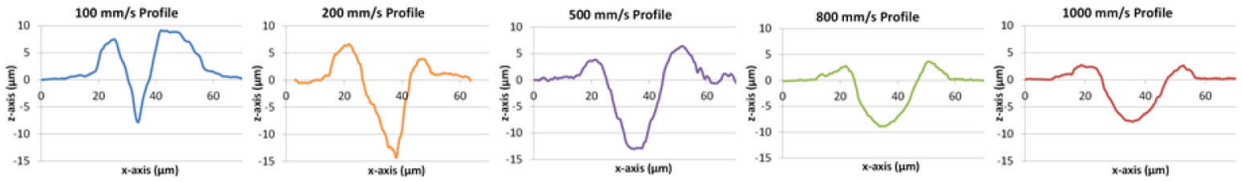


**Figure 4.** Profile data from the 3D optical microscope for scanning speeds of 100, 200, 500, 800, and 1000 mm/s at an overlap number of 1, a power of 15 W, and a frequency of 100 kHz.

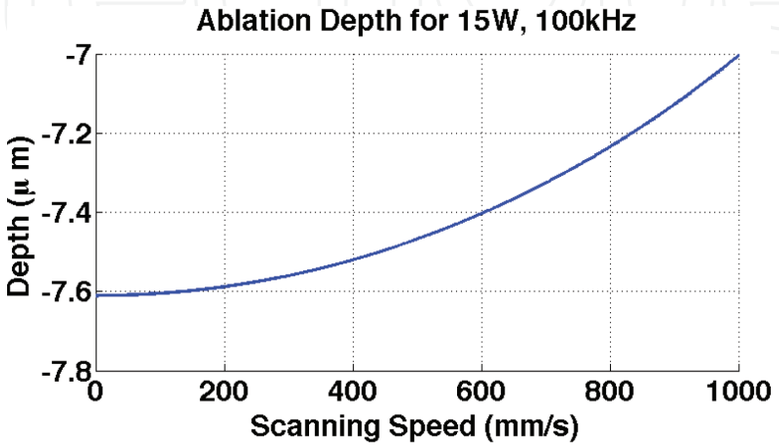


**Figure 5.** Ablation depth after a train of pulses at difference scanning speeds at a power of 15 W and a frequency of 100 kHz.

sides of the groove. At higher scanning speeds, when the pulses are farther apart, there is less penetration on the surface, leading to a shallower groove. At lower scanning speeds, the high-temperature ablated material from the walls caves back into the deep groove and solidifies into a much shallower groove than initially dredged. Scanning speeds of 200 and 800 mm/s show a deep groove with a smaller amount of material built up than the 100 mm/s sample.

Eqs. (6) and (7) are then used to find the theoretical ablation depths at various scanning speeds. Observing the trend in **Figure 5**, it is clear that the ablation depth decreases with increasing scanning speed. Both the experimental data and theoretical results are in close agreement.

### 3.2. Bioactivity assessment

Each sample was submerged in simulated body fluid (SBF) for 6 weeks and kept at a constant temperature of 36.5°C. The samples were then emerged from the fluid and assessed with energy-dispersive X-ray (EDX). The SBF-soaked samples were found to contain a traces of phosphorous and calcium, which is indicative of the presence of a bone-like apatite. Hydroxy-apatite is formed by the nucleation of calcium phosphate ions [5, 27]. The silicon oxide layer created by the laser plume has a negative charge, which attracts the positively charged calcium phosphate. The resulting substrate contains this bone-like apatite, which was seen on the laser-treated silicon samples. The EDX results from the sample with three overlap and 0.025 mm line spacing can be seen in **Figure 6**.

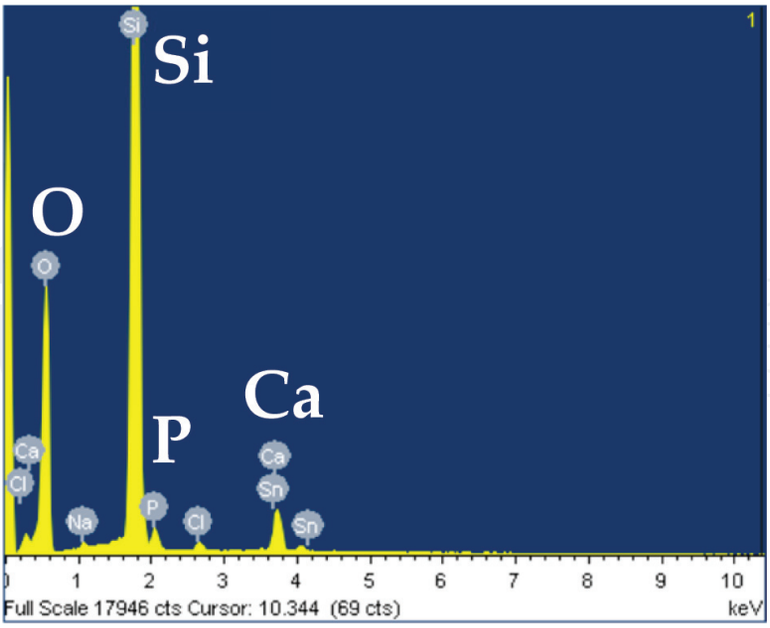


**Figure 6.** EDX results of sample with three overlaps, 0.025 mm line spacing, 400 mm/s, a power of 13.3 W, and a frequency of 400 mm/s.

This presence of bone-like apatite confirms that the biocompatibility of pure silicon was enhanced with nanosecond laser pulses. A smaller line spacing and higher overlap number generates more $SiO_2$ nanofibers, which provides a favorable site for the nucleation of apatite.

## 4. Effect of frequency

The range of frequencies used in this section is 25, 70, and 100 kHz. For these experiments, the scanning speed was kept constant at 100 mm/s, the power at 15W, and the overlap number at 1.

### 4.1. Topography analysis

**Figures 7** and **8** show the topography changes in the frequency samples. A lower frequency produces a wider and shallower groove, while the higher frequencies yield a thinner yet deeper ablated groove. The theoretical results in for a single pulse in **Figure 9** show that the groove increases in depth and decreases in width as frequency increases, which is in close agreement with the experimental results.

### 4.2. Temperature analysis

The temperature is determined for each frequency with Eq. (3) and can be found in **Figure 10**. The higher temperatures are associated with the lower frequencies on both z-axis and r-axis. By increasing the frequency, the pulse energy decreases which results in lower temperatures and a smaller heat-affected zone [30]. Due to reduced size of the heat-affected zone, the shape of the groove consequently changes size as well. This results in the thinner grooves at higher

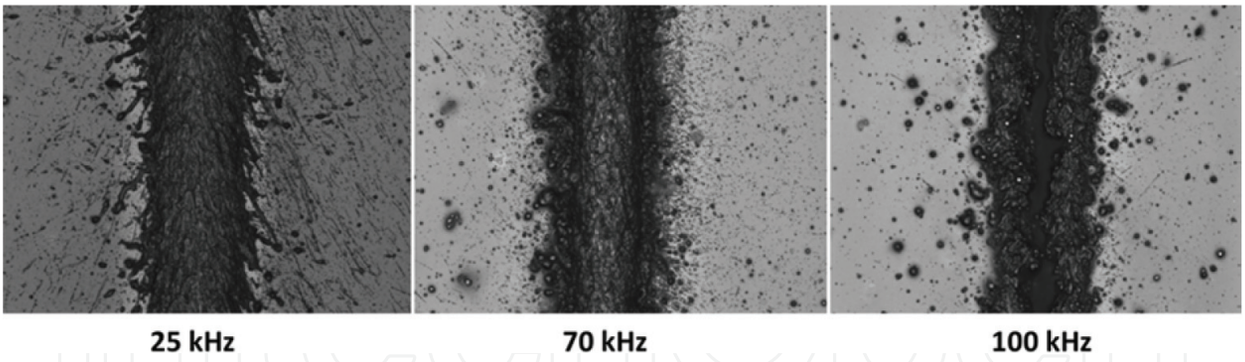


**Figure 7.** 3D optical microscopy images of samples with frequencies of 25, 70, and 100 kHz at a power of 15 W, a scanning speed of 100 mm/s, and 1 overlap.

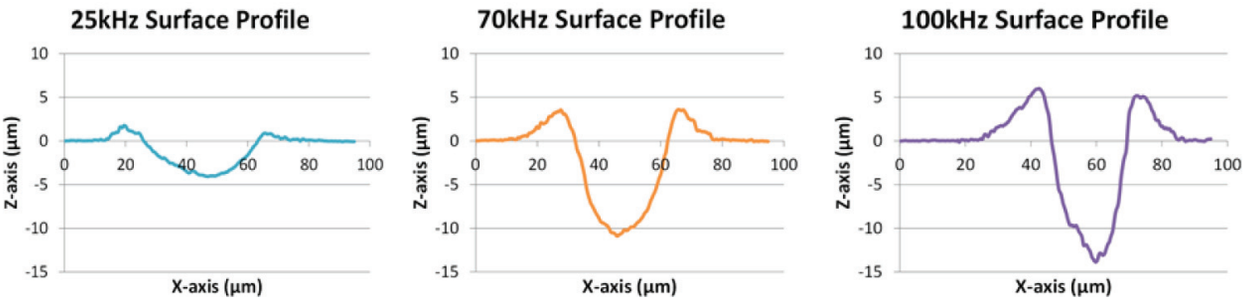


**Figure 8.** Experimental profile data from the 3D optical microscope for frequencies of 25, 70, and 100 kHz at an overlap number of 1, a power of 15 W, and a scanning speed of 100 mm/s.

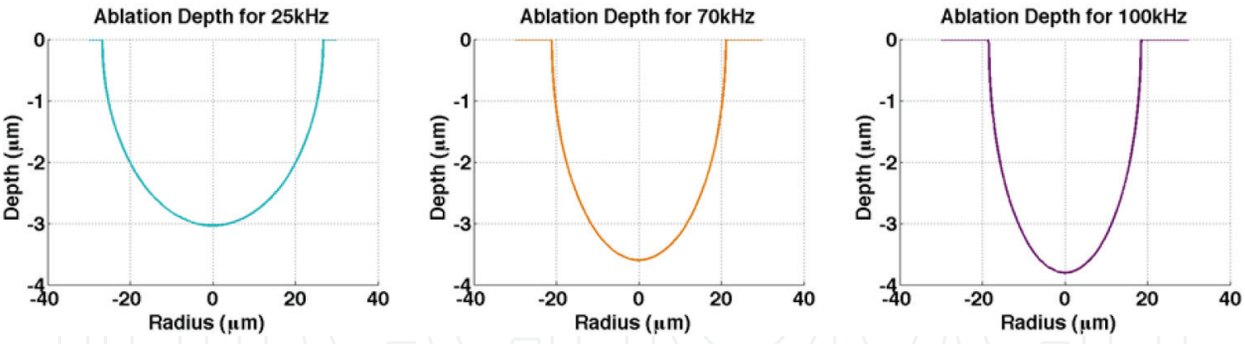


**Figure 9.** Theoretical profile data for a single pulse for frequencies of 25, 70, and 100 kHz at an overlap number of 1, a power of 15 W, and a scanning speed of 100 mm/s.

frequencies. Each recurring pulse adds to the penetration of preceding pulse. Higher frequencies have more pulses, resulting in a deeper penetration of the surface, which develops a trench with a larger depth.

### 4.3. Bioactivity assessment

Mouse embryonic fibroblast cell interactions were examined for each frequency. The cell count in **Figure 11** establishes that there are a higher number of cells in the higher frequency grooves.

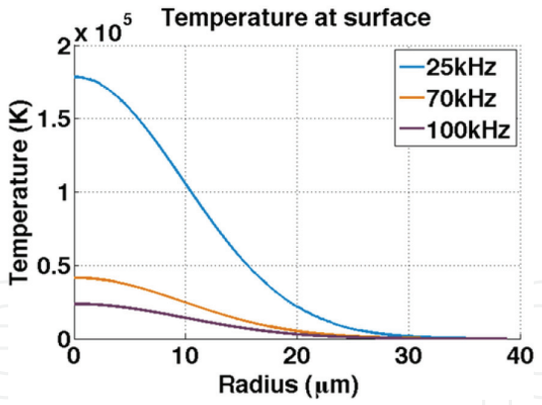


**Figure 10.** The single-pulse temperature on the surface of the silicon with respect to radius.

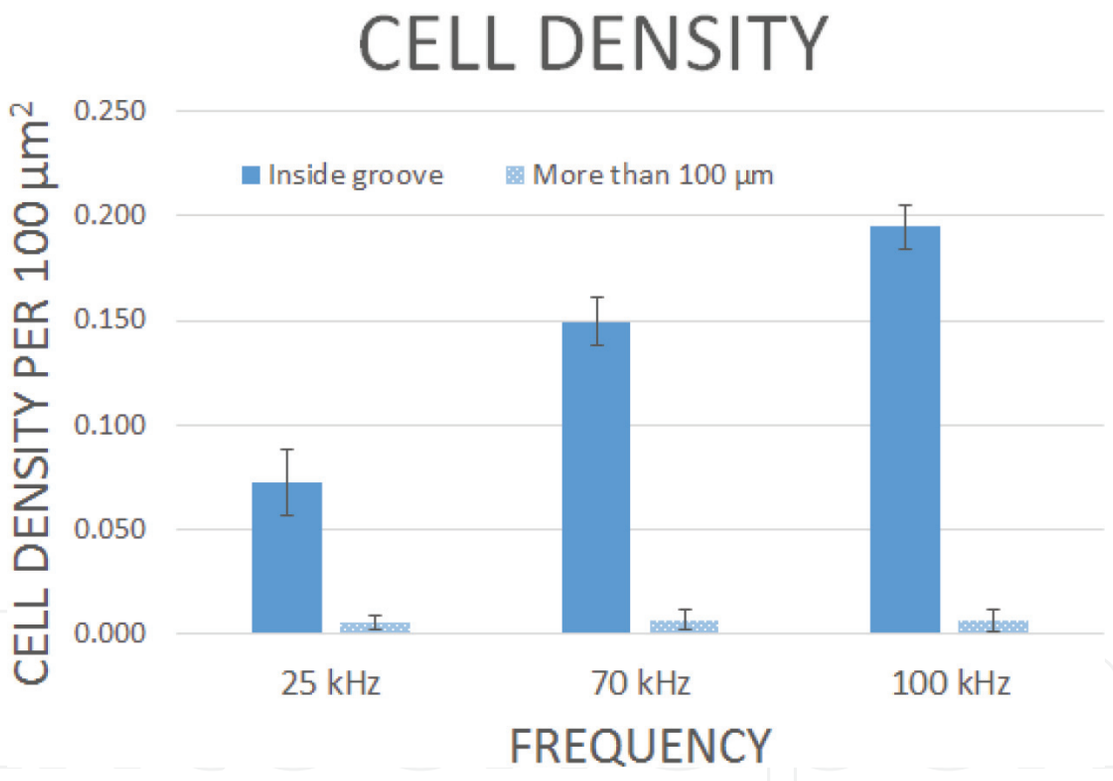


**Figure 11.** The number of cells within the laser-treated groove for each frequency as well as the amount of cells outside the groove within 100 μm from the edge of the groove [30].

The cells show a strong preference for the treated areas and show avoidance in the untreated areas. There is also a presence of fibronectin within the cells, which is an ECM protein secreted during embryonic development and wound healing, potentially leading to collagen deposition and tissue morphogenesis [30, 31]. These results confirm that the biocompatibility is enhanced with higher frequencies.

## 5. Effect of power

Laser power immensely influences the surface properties when treatment is done to a material. The power for this section varies from 7, 10 to 15 W. For these experiments, the frequency was kept constant at 100 kHz, the scanning speed was set to 400 mm/s, and the overlap number was 1.

### 5.1. Topography analysis

The FESEM images of each power sample are shown in **Figure 12**. The experimental 3D optical microscopy profile data is shown in **Figure 13**. These results show that at higher powers, the groove will increase in both width and depth. Unlike the frequency trends, the size of the heat-affected zone increases with power. The theoretical single-pulse depths found with Eq. (5) are shown in **Figure 14**. These results also show that the groove width and depth increase with power and are in close agreement with the experimental results.

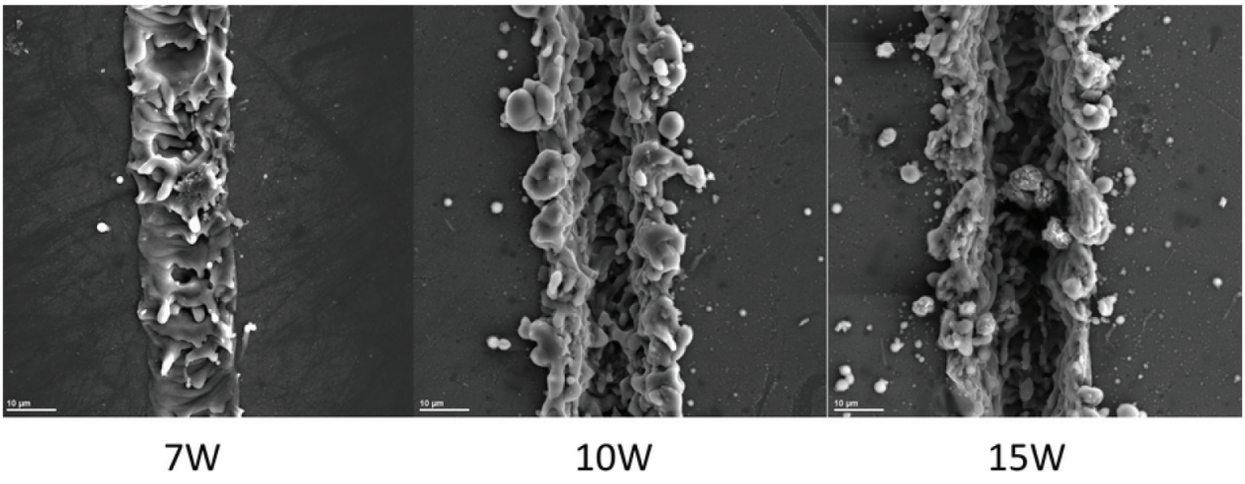


**Figure 12.** FESEM images of samples with powers of 7, 10, and 15 W at a frequency of 100 kHz, a scanning speed of 400 mm/s, and 1 overlap.

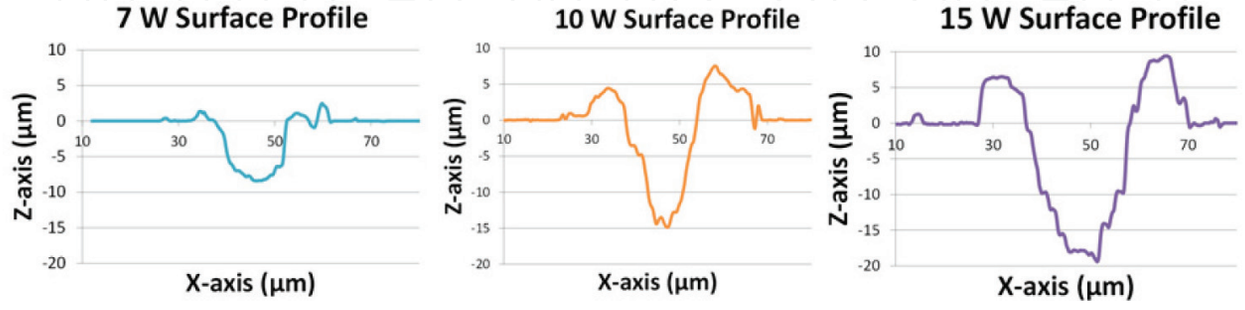


**Figure 13.** Experimental profile data from the 3D optical microscope for powers of 7, 10, and 15 W at an overlap number of 1, a frequency of 100 kHz, and a scanning speed of 400 mm/s.

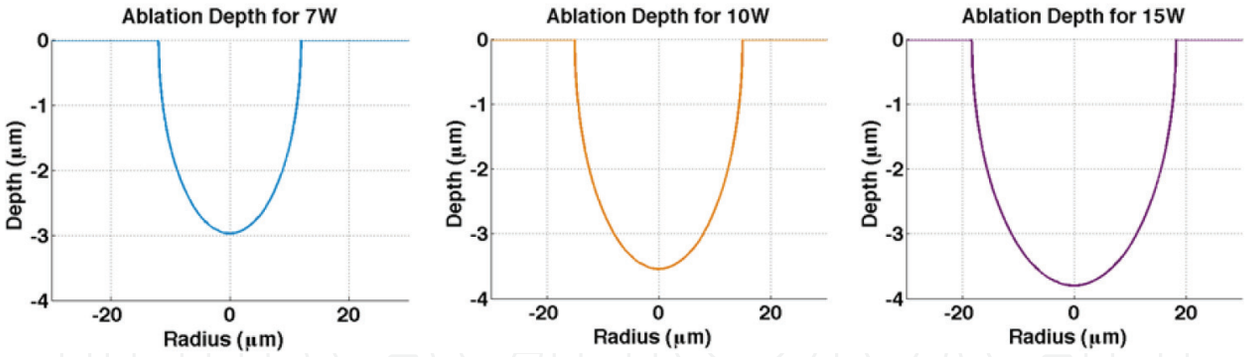


**Figure 14.** Theoretical profile data for a single pulse for powers of 7, 10, and 15 W with an overlap number of 1, a frequency of 100 kHz, and a scanning speed of 400 mm/s.

### 5.2. Temperature analysis

The temperature is determined for each power with Eq. (3) and can be found in **Figure 15**. As expected, the higher temperatures are found with higher powers. At lower powers, the heat-affected zone is smaller, allowing for both a thinner and shallower groove. When the pulse power is increased, the temperatures in the high-density plume are increased, causing more generation of the $SiO_2$ nanofibers [26].

### 5.3. Bioactivity assessment

Samples were once again assessed with fibroblast culturing for each power. When viewing the cell interactions under the microscope, cells were accumulated inside the laser-treated area as expected. Interestingly, the cell count was low directly beside the grooves and began to become more concentrated farther away from the edge of the groove. The fibroblasts avoided the zones immediately beside the grooves on each side. This can be seen in **Figure 16**.

This phenomenon is a result from the shockwave that is generated from the high-energy plume during laser ablation [26]. The shockwave transfers energy to the surface with results in high intensity thermal stress. The thermal shock causes a small zone directly beside the

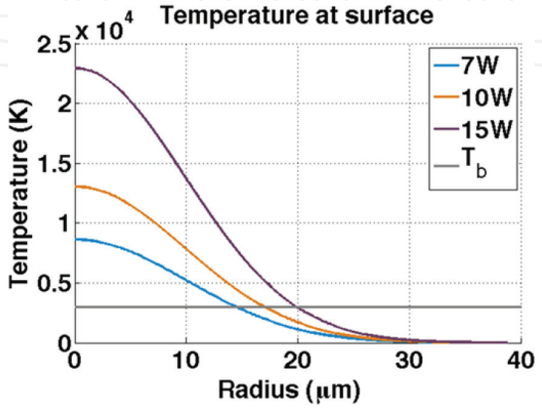


**Figure 15.** The single-pulse temperature on the surface of the silicon with respect to radius. $T_b$ is the boiling temperature of silicon at 3538 K.

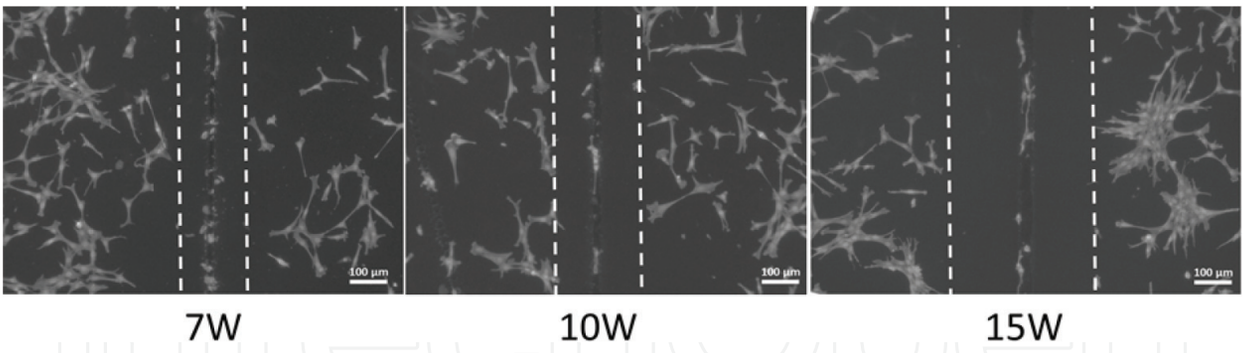


**Figure 16.** Fibroblast cells avoiding the zones beside the grooves for powers of 7, 10, and 15 W.

ablated areas, which contains residual stress. When the power is increased, there is a larger transfer energy, resulting in a larger stress zone. These residual stress zones contain mismatched crystal orientations due to tensile stresses causing crystal distortion.

Knowing that the power level of the laser pulse can control the residual stress zone size and cell behavior, this research can provide opportunities in cell manipulation and cell programming.

## 6. Summary

This chapter aims to introduce nanosecond laser processing for the enhancement of biocompatibility of pure silicon for various biomedical technologies. These results can contribute to the design of manufacturing processes of innovative biomedical devices to enhance the quality of living for a number of individuals. This research investigates the trends of various laser parameters including three scanning parameters (line spacing, overlap number, and scanning speed), pulse frequency, and laser power. Biocompatible *in vitro* assessment was conducted through the use of simulated body fluid (SBF) and cell culturing with NIH 3T3 fibroblasts. Samples with smaller line spacing and higher overlap numbers showed more generation of $SiO_2$ nanofibers, which were shown to be biocompatible under SBF assessment. Biocompatibility increased with frequency due to the $SiO_2$ being more prominent on high frequency samples and containing more fibroblast cell proliferation. Fibroblasts also showed preference to higher powers. However, the heat-affected zone immediately outside the ablated areas showed a mismatch of crystal orientations causing residual stress. These stress zones were avoided by cells, which led to promising results for the potential in cell programming and manipulation.

## Author details

Candace Colpitts and Amirkianoosh Kiani*

*Address all correspondence to: a.kiani@unb.ca

Silicon Hall: Laser Micro/Nanofabrication Facility, Department of Mechanical Engineering, University of New Brunswick, NB, Canada

## References


[1] Turner AP, Pickup JC. Diabetes mellitus: Biosensors for research and management. Biosensors. 1985;**1**(1):85-115

[2] Grayson AR, et al. A BioMEMS review: MEMS technology for physiologically integrated devices. Proceedings of the IEEE. 2004;**92**(1):6-21

[3] Copeland JG, et al. Cardiac replacement with a total artificial heart as a bridge to transplantation. The New England Journal of Medicine. 2004;**351**(9):859-867

[4] Li X, et al. The use of nanoscaled fibers or tubes to improve biocompatibility and bioactivity of biomedical materials. Journal of Nanomaterials. 2013;**2013**:14

[5] Radmanesh M, Kiani A. Effects of laser pulse numbers on surface biocompatibility of titanium for implant fabrication. Journal of Biomaterials and Nanobiotechnology. 2015; **6**:168

[6] Swetha M, et al. Biocomposites containing natural polymers and hydroxyapatite for bone tissue engineering. International Journal of Biological Macromolecules. 2010;**47**(1):1-4

[7] Yue Z, et al. Controlled delivery for neuro-bionic devices. Advanced Drug Delivery Reviews. 2013;**65**(4):559-569

[8] Vallet-Regí M, Colilla M, González B. Medical applications of organic–inorganic hybrid materials within the field of silica-based bioceramics. Chemical Society Reviews. 2011;**40**(2): 596-607

[9] Green ML, et al. Ultrathin (<4 nm) $SiO_2$ and Si–O–N gate dielectric layers for silicon microelectronics: Understanding the processing, structure, and physical and electrical limits. The Journal of Applied Physics. 2001;**90**(5):2057-2121. DOI: http://dx.doi.org/10.1063/1.1385803

[10] Jeong S, et al. Hybrid silicon nanocone-polymer solar cells. Nano Letters. 2012;**12**(6): 2971-2976. Available: http://dx.doi.org/10.1021/nl300713x. DOI: 10.1021/nl300713x

[11] Buckberry L, Baylis S. Porous silicon as a biomaterial. Materials World. 1999;**7**:213-215

[12] Shaoqiang C, et al. Hydroxyapatite coating on porous silicon substrate obtained by precipitation process. Applied Surface Science. 2004;**230**(1):418-424

[13] Mwenifumbo S, et al. Cell/surface interactions on laser micro-textured titanium-coated silicon surfaces. The Journal of Materials Science: Materials in Medicine. 2007;**18**(1):9-23

[14] Myllymaa S, et al. Adhesion, spreading and osteogenic differentiation of mesenchymal stem cells cultured on micropatterned amorphous diamond, titanium, tantalum and chromium coatings on silicon. Journal of Materials Science: Materials in Medicine. 2010;**21**:329-341

[15] Vilhena LM, et al. Surface texturing by pulsed Nd:YAG laser. Tribology International. 2009;**42**(10):1496-1504. DOI: dx.doi.org/10.1016/j.triboint.2009.06.003

[16] Radmanesh M, Kiani A. Nd: YAG laser pulses ablation threshold of stainless steel 304. Materials Sciences and Applications. 2015;**6**(07):634

[17] Bonse J, et al. Femtosecond laser ablation of silicon–modification thresholds and morphology. Applied Physics A. 2002;**74**(1):19-25

[18] Kiani A, et al. Leaf-like nanotips synthesized on femtosecond laser-irradiated dielectric material. The Journal of Applied Physics. 2015;**117**(7):074306

[19] Wood JP, et al. Nanosecond pulse lasers for retinal applications. Lasers in Surgery and Medicine.2011;**43**(6):499-510

[20] Al-Hadeethi Y, et al. Data fitting to study ablated hard dental tissues by nanosecond laser irradiation. PLoS One. 2016;**11**(5):e0156093

[21] Khademhosseini A, et al. Microscale technologies for tissue engineering and biology. Proceedings of the National Academy of Sciences of the United States of America. 2006;**103**(8):2480-2487. DOI: 0507681102 [pii]

[22] Canham LT. Bioactive silicon structure fabrication through nanoetching techniques. Advanced Materials. 1995;**7**(12):1033-1037

[23] Kamitakahara M, et al. Bioactivity and mechanical properties of polydimethylsiloxane (PDMS)-CaO-$SiO_2$ hybrids with different PDMS contents. The Journal of Sol-Gel Science and Technology. 2001;**21**(1-2):75-81

[24] Incropera FP, et al. Introduction to convection. In: Anonymous, editors. Introduction to Heat Transfer. 5th ed. Danvers, MA, USA: John Wiley & Sons; 2007. pp. 57

[25] Hendow ST, Shakir SA. Structuring materials with nanosecond laser pulses. Optics Express. 2010;**18**(10):10188-10199

[26] Tavangar A, Tan B, Venkatakrishnan K. Study of the formation of 3-D titania nanofibrous structure by MHz femtosecond laser in ambient air. The Journal of Applied Physics. 2013;**113**(2):023102

[27] Tavangar A, Tan B, Venkatakrishnan K. The influence of laser-induced 3-D titania nanofibrous platforms on cell behavior. Journal of biomedical nanotechnology. 2013;**9**(11):1837-1846

[28] Kiani A, Venkatakrishnan K, Tan B. Optical absorption enhancement in 3D nanofibers coated on polymer substrate for photovoltaic devices. Optics Express. 2015;**23**(11):A569-A575

[29] Colpitts C, Kiani A. Synthesis of bioactive three-dimensional silicon-oxide nanofibrous structures on the silicon substrate for bionic devices' fabrication. Nanotechnology and Nanomaterials. 2016;**6**:1-7

[30] Colpitts C, et al. Mammalian fibroblast cells show strong preference for laser-generated hybrid amorphous silicon-$SiO_2$ textures. Journal of Applied Biomaterials and Functional Materials. 2016. DOI: D2673E51-9D76-4504-A673-13AAC5CE7AD3 [pii]

[31] Vega ME, Schwarzbauer JE. Collaboration of fibronectin matrix with other extracellular signals in morphogenesis and differentiation. Current Opinion in Cell Biology. 2016;**42**:1-6. DOI: S0955-0674(16)30055-2 [pii]

IntechOpen